IEEE Access
Multidisciplinary | Rapid Review | Open Access Journal

Received April 5, 2019, accepted May 4, 2019, date of publication May 17, 2019, date of current version June 3, 2019.

Digital Object Identifier 10.1109/ACCESS.2019.2917533

Stability Enhancement for Parallel Grid-Connected Inverters by Improved Notch Filter

LING YANG[1], (Student Member, IEEE), YANDONG CHEN[1], (Senior Member, IEEE), AN LUO[1], (Senior Member, IEEE), AND KUNSHAN HUAI[2]

[1]College of Electrical and Information Engineering, Hunan University, Changsha 410082, China
[2]Guangzhou Power Supply Co., Ltd., Guangzhou 510620, China

Corresponding author: Yandong Chen (yandong_chen@hnu.edu.cn)

This work was supported in part by the National Key R&D Program of China under Grant 2017YFB0902000, and in part by the Science and Technology Project of State Grid under Grant SGXJ0000KXJS1700841.

ABSTRACT As parallel inverters connected to the weak grid, the interactions between the inverters and the grid are the potential threat to the system stability. The traditional grid-side inductance current feedback control method with notch filter can suppress the high-frequency oscillation. However, it will lead to stability reduction and even instability. Therefore, a stability enhancement method by the improved notch filter is proposed for parallel grid-connected inverters. This method can effectively restrain parallel inverters' harmonic current into the grid, and accordingly avoid the high-frequency oscillation of impedance network. Furthermore, it improves the phase margin of the system, and thus ensures the sufficient stability of the system in the weak grid. Considering the notch depth and dynamic performance of improved notch filter, the appropriate control parameters are selected. Finally, experimental results verify the validity of the proposed control method.

INDEX TERMS Weak grid, parallel inverters, improved notch filter, impedance reshaping, stability enhancement.

I. INTRODUCTION

Renewable energy generations are continuously increasing due to their convenience and flexibility for access to the grid [1], [2], which include small-scale distributed generations and medium to large-scale power plants. The former case is to promote the development of renewable energies by optimizing the utilization of decentralized renewable energies [3]. The latter case becomes an important trend of renewable energy industry for high efficiency and centralized management [4]. Due to the scattered location of renewable energy generations, long transmission lines are used to connect the system to the public grid [5], [6]. Therefore, the public grid shows the characteristics of weak grid in which the grid impedance cannot be neglected [7], [8].

Especially, renewable energies are mostly connected to the grid by parallel inverters [9], [10]. In this way, the distributed generations and power plants can easily increase the output power, and it is convenient to perform the redundancy operation [11], [12]. However, parallel inverters are unfortunately coupled with the grid due to the presence of grid impedance [13]. The coupling interactions between the inverters and the grid may cause the oscillation and aggravate the instability problems [14].

There are there kinds of methods to improve the stability of multi-inverter grid-connected system. The first is from the perspective of equivalent circuit model [15]–[17]. References [15], [16] proposed the harmonic mathematical model of high-frequency domain, and revealed the mechanism of high-frequency oscillation. Reference [17] established the mathematical model of fundamental frequency domain, and analyzed the coupling interactions of impedance network.

The second one is to reconstruct the grid impedance [18]. An active damper was proposed to suppress the high-frequency oscillation in [18], which could be plug-and-play interfaced to form complete system for particular needs. However, this method requires additional hardware, which improves the cost of the system and reduces the reliability of the system [19].

The associate editor coordinating the review of this manuscript and approving it for publication was Atif Iqbal.

The third one is to reshape the inverter output impedance [20], [21]. Reference [20] proposed an active damping method based on cascaded notch filter to ensure the system stability. Reference [21] used the notch filter to filter out the fundamental component of grid-connected current, and then fed back to the command current. Therefore, the high-frequency inverter output impedance was reshaped to suppress the oscillation in a certain extent. However, due to the large negative phase shift near the characteristic frequency of notch filter, the phase margin of the system is decreased, resulting in the system stability is reduced.

In this paper, a stability enhancement method by the improved notch filter is proposed for parallel grid-connected inverters. This paper is organized as follows. Section II qualitatively analyzes the oscillation reason in multi-inverter grid-connected system. Section III gives the inverter output impedance and studies the reasons for the system instability under the traditional control method. Section IV proposes the stability enhancement method by improved notch filter, comparatively analyzes the system performances between the traditional control method and proposed control method, and gives the parameters design of improved notch filter. Section V provides the experimental results to verify the validity of proposed control method. Finally, Section VI gives some conclusions.

II. QUALITATIVE ANALYSIS OF OSCILLATION REASON IN MULTI-INVERTER GRID-CONNECTED SYSTEM

The structure of multi-inverter grid-connected system is shown in Fig. 1. The photovoltaic array and DC/DC converter are connected to the public grid through LCL-type grid-connected inverter. $j = 1, 2, \cdot\cdot, n$. Capacitor $C_{\mathrm{d}j}$, inductor $L_{\mathrm{dc}j}$ and two power transistors make up the DC/DC converter. The DC-side capacitor $C_{\mathrm{dc}j}$ is used to stabilize the DC-side voltage $u_{\mathrm{dc}j}$. The inverter-side inductor L_{1j}, filter capacitor C_{1j} and grid-side inductor L_{2j} constitute the LCL filter. $R_{\mathrm{L}1j}$ and $R_{\mathrm{L}2j}$ are parasitic resistances of L_{1j} and L_{2j}. $u_{\mathrm{in}j}$ is the input voltage. $u_{\mathrm{C}1j}$ is the filter capacitor voltage. u_{PCC} is the PCC voltage. u_{g} is the grid voltage. Z_{g} is the grid impedance. $i_{\mathrm{Ldc}j}$, $i_{\mathrm{ot}j}$ and $i_{\mathrm{dc}j}$ are the DC-side inductor current, DC-side output current and AC-side input current. $i_{\mathrm{L}1j}$, $i_{\mathrm{C}1j}$, $i_{\mathrm{o}j}$ and i_{g} are the inverter-side inductor current, filter capacitor current, grid-side inductor current and grid-connected current.

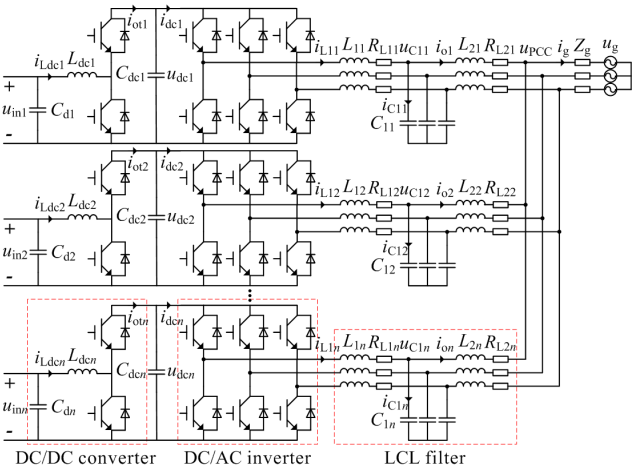

FIGURE 1. Structure of multi-inverter grid-connected system.

Considering the effect of nonlinear factors such as dead-time of switching devices in the grid-connected inverter, the effect can be regarded as a controlled current source in the Norton equivalent circuit [22]. Therefore, the single inverter is equivalent to the current source i_j (ideal current source i_{1j} and controlled current source $i_{\mathrm{d}j}$) in parallel with equivalent admittance Y_j. In addition, the grid is equivalent to the grid voltage u_{g} in series with grid impedance Z_{g}. Starting from the PCC, the Norton equivalent circuit of single inverter is connected in parallel, which forms the Norton equivalent circuit of multi-inverter grid-connected system, as shown in Fig. 2(a). Moreover, the output admittance model of multi-inverter grid-connected system is shown in Fig. 2(b).

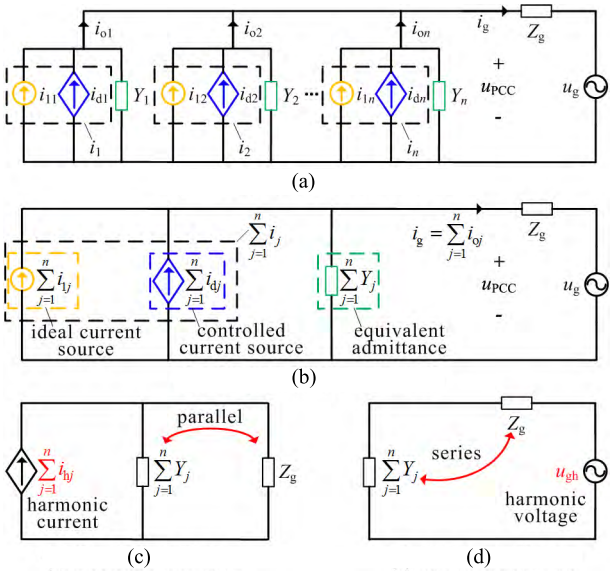

FIGURE 2. Qualitative analysis of high-frequency oscillation reason in multi-inverter grid-connected system. (a) The Norton equivalent circuit. (b) Output admittance model. (c) Parallel oscillation. (d) Series oscillation.

In Fig. 2(c), the harmonic current $i_{\mathrm{h}j}$ is caused by the nonlinear factors of the inverters. If the frequency of the harmonic current equals or closes to the parallel resonant frequency of impedance network, the parallel oscillation will occur. In Fig. 2(d), the harmonic voltage u_{gh} is introduced by the grid distortion. If the frequency of the harmonic voltage equals or closes to the series resonant frequency of impedance network, it will cause the series oscillation.

Therefore, there are two indispensable conditions for the oscillation: one is the existence of resonance network, the other is the harmonic source. Therefore, preventing harmonics from flowing into the resonance network is one of the suppression oscillation methods.

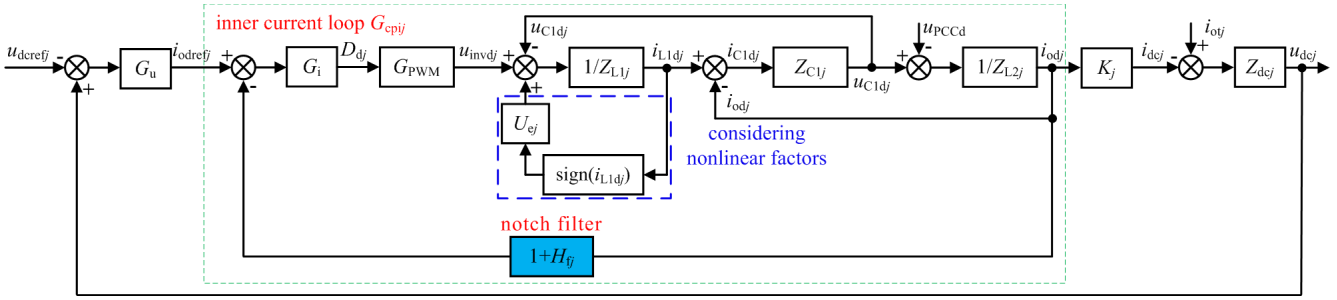

FIGURE 3. Control block diagram of traditional control method by the notch filter.

III. TRADITIONAL OSCILLATION SUPPRESSION METHOD BY NOTCH FILTER

A. BASIC PRINCIPLES OF TRADITIONAL CONTROL METHOD

The control block diagram of traditional control method by the notch filter is shown in Fig. 3. The active current reference value i_{odref} is obtained from the outer voltage loop, and the reactive current reference value i_{oqref} is directly obtained from the reactive power control target. Taking the d-axis as an example, the traditional control method introduces the notch filter to the grid-side inductor current feedback, which suppresses the harmonic current of parallel inverters from flowing into the grid. In Fig. 3, u_{dcrefj} is the DC-side voltage reference, G_u is the outer voltage loop PI controller, G_i is the inner current loop PI controller, G_{PWM} is the equivalent gain of the inverter, K_j is the proportional gain, H_{fj} is the grid-side inductor current feedback coefficient, $Z_{L1j} = sL_{1j} + R_{L1j}$, $Z_{C1j} = 1/(sC_{1j})$, $Z_{L2j} = sL_{2j} + R_{L2j}$ and $Z_{dcj} = 1/(sC_{dcj})$.

The effect of nonlinear factors can be regarded as the disturbance in the grid-connected inverter. The amplitude of the disturbance is constant, and the direction of the disturbance is related to the inverter-side inductor current [21]. Therefore, the disturbance signal can be regarded as the controlled current source i_{dj} in the Norton equivalent circuit, which can be expressed as

$$i_{dj} = \frac{U_{ej}}{A+B+C} \cdot \text{sign}(i_{L1dj}) \tag{1}$$

where $U_{ej} = 2(U_{dcj} + U_{Dj} - U_{Tj})\frac{t_{dj}+t_{onj}-t_{offj}}{T_{sj}} - U_{Dj} - U_{Tj}$, U_{Tj} and U_{Dj} are the turn-on voltage drop of the switching device and diode, T_{sj}, t_{dj}, t_{onj} and t_{offj} are the switching period, dead time, on-time and off-time of the switching device, $\text{sign}(i_{L1dj}) = \begin{cases} 1 & i_{L1dj} > 0 \\ -1 & i_{L1dj} < 0 \end{cases}$, $A = Z_{L1j}Z_{L2j}$, $B = (1 + H_{fj})G_iG_{PWM}Z_{C1j}$, and $C = Z_{C1j}(Z_{L1j} + Z_{L2j})$.

Ignoring the inverter losses, the power input from the system to the grid can be expressed as

$$p_{gj} = u_{dcj}i_{dcj} = 1.5u_{PCCd}i_{odj} \tag{2}$$

where p_{gj} is the AC-side power, u_{PCCd} is the d-axis component of PCC voltage, and i_{odj} is the d-axis component of grid-side inductor current.

From (2), the proportional gain K_j can be expressed as

$$K_j = \frac{i_{dcj}}{i_{odj}} = \frac{1.5u_{PCCd}}{U_{dcj}} \tag{3}$$

where U_{dcj} is the steady-state value of DC-side voltage.

In order to ensure that the DC-side voltage is constant, it is necessary to perform closed-loop control on the DC-side voltage u_{dc}.

From Fig. 3, the closed-loop transfer function of the inner current loop can be expressed as

$$i_{odj} = G_{cpij}i_{odrefj} + i_{dj} - Y_{cpij}u_{PCCd} \tag{4}$$

where G_{cpij} is the equivalent coefficient of inner current loop, and Y_{cpij} is the equivalent admittance of inner current loop. The both can be expressed as

$$\begin{cases} G_{cpij} = \dfrac{G_iG_{PWM}Z_{C1j}}{A+B+C} \\ Y_{cpij} = \dfrac{Z_{L1j}+Z_{C1j}}{A+B+C} \end{cases} \tag{5}$$

The equivalent control block diagram of traditional control method is shown in Fig. 4, where Z_{sj} is the series virtual impedance, $Z_{sj} = r_1G_N$, r_1 is the proportional coefficient, and G_N is the notch filter. The traditional control method is equivalent to connecting the virtual impedance in series with the inverter output impedance, which suppresses the high-frequency oscillation.

From Fig. 4, the equivalent closed-loop transfer function of the inner current loop can be expressed as

$$i_{odj} = G_{cpieqj}i_{odrefj} + i_{dj} - Y_{cpieqj}u_{PCCd} \tag{6}$$

where G_{cpieqj} is the inner-current-loop equivalent coefficient after transformation, and Y_{cpieqj} is the inner-current-loop equivalent admittance after transformation. The both can be expressed as

$$\begin{cases} G_{cpieqj} = \dfrac{G_iG_{PWM}Z_{C1j}}{D+Z_{sj}E} \\ Y_{cpieqj} = \dfrac{Z_{L1j}+Z_{C1j}}{D+Z_{sj}E} \end{cases} \tag{7}$$

where $D = Z_{L1j}Z_{L2j} + Z_{C1j}(G_iG_{PWM} + Z_{L1j} + Z_{L2j})$, and $E = Z_{L1j} + Z_{C1j}$.

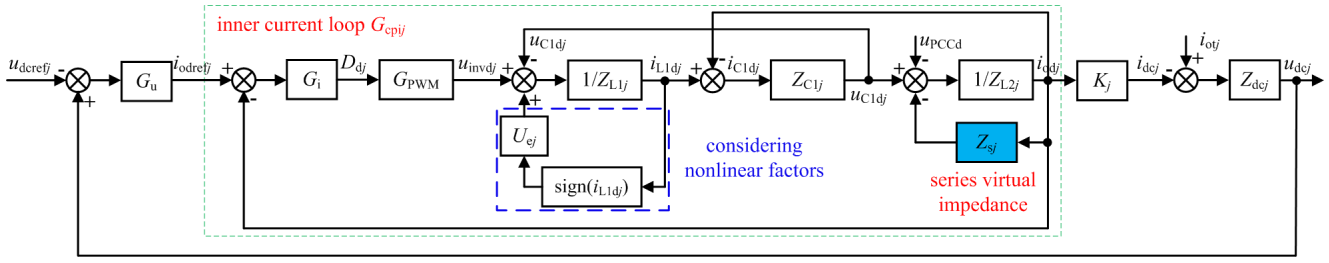

FIGURE 4. Equivalent control block diagram of traditional control method by the notch filter.

To achieve the same target for Fig. 4 and Fig. 3, the current source equivalent coefficient and equivalent admittance in (7) should be designed equal to the corresponding expressions in (5), which is expressed as

$$\begin{cases} G_{\mathrm{cpi}j} = G_{\mathrm{cpieq}j} \\ Y_{\mathrm{cpi}j} = Y_{\mathrm{cpieq}j} \end{cases} \tag{8}$$

From (8), the grid-side inductor current feedback coefficient H_{fj} can be expressed as

$$H_{\mathrm{f}j} = \frac{r_1 G_{\mathrm{N}}(Z_{\mathrm{L1}j} + Z_{\mathrm{C1}j})}{G_{\mathrm{i}} G_{\mathrm{PWM}} Z_{\mathrm{C1}j}} \tag{9}$$

The notch filter G_N can be expressed as

$$G_{\mathrm{N}} = \frac{(\frac{s}{2\pi f_{\mathrm{o}}})^2 + 2k_1 \frac{s}{2\pi f_{\mathrm{o}}} + 1}{(\frac{s}{2\pi f_{\mathrm{o}}})^2 + 2k_2 \frac{s}{2\pi f_{\mathrm{o}}} + 1} \tag{10}$$

where f_o is the characteristic frequency (ie, the fundamental frequency), and k_1 and k_2 are the proportional coefficient, which are related to the bandwidth and notch depth of the notch filter.

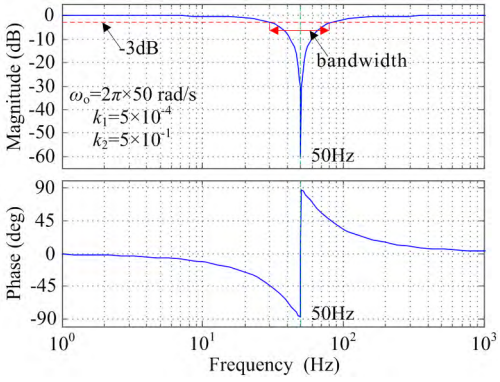

FIGURE 5. The Bode diagram of the notch filter G_N.

The Bode diagram of the notch filter G_N is shown in Fig. 5, where ω_o is the characteristic angular frequency (i.e., the fundamental angular frequency), $\omega_o = 2\pi f_o = 2\pi \times 50$rad/s, $k_1 = 5 \times 10^{-4}$, and $k_2 = 5 \times 10^{-1}$. The bandwidth of notch filter is 50Hz and the notch depth of notch filter is -60dB. If the grid-side inductor current passes through the notch filter, the fundamental frequency component of the current will be greatly attenuated, and the other frequencies components of the current will pass almost non-destructively. The function is to extract other frequencies components except the fundamental frequency component for the impedance reshaping. However, the large negative phase shift near the characteristic frequency of notch filter is introduced, which causes the certain limitations of traditional control method. The adverse effects of the notch filter in the traditional control method on the system stability are analyzed in Section III.C.

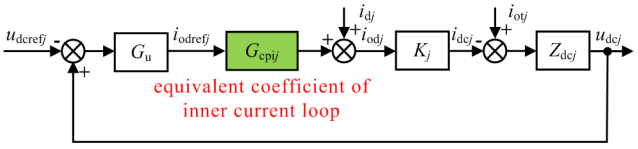

FIGURE 6. Simplified control block diagram of traditional control method.

The simplified control block diagram of traditional control method is shown in Fig. 6. As can be seen from Fig. 6, the double closed-loop transfer function of the system can be expressed as

$$u_{\mathrm{dc}j} = G_{\mathrm{cpd}j} u_{\mathrm{dcref}j} + Z_{\mathrm{d}j} i_{\mathrm{d}j} - Z_{\mathrm{cpd}j} i_{\mathrm{ot}j} \tag{11}$$

where G_{cpdj} is the equivalent coefficient of the double closed loop, Z_{cpdj} is the equivalent impedance of the double closed loop, and Z_{dj} is the equivalent impedance of controlled current source. They can be expressed as

$$\begin{cases} G_{\mathrm{cpd}j} = \dfrac{G_{\mathrm{opd}j}}{1 + G_{\mathrm{opd}j}} = \dfrac{G_{\mathrm{u}} G_{\mathrm{cpi}j} K_j Z_{\mathrm{dc}j}}{1 + G_{\mathrm{u}} G_{\mathrm{cpi}j} K_j Z_{\mathrm{dc}j}} \\ Z_{\mathrm{cpd}j} = \dfrac{Z_{\mathrm{dc}j}}{1 + G_{\mathrm{u}} G_{\mathrm{cpi}j} K_j Z_{\mathrm{dc}j}} \\ Z_{\mathrm{d}j} = \dfrac{K_j Z_{\mathrm{dc}j}}{1 + G_{\mathrm{u}} G_{\mathrm{cpi}j} K_j Z_{\mathrm{dc}j}} \end{cases} \tag{12}$$

where G_{opdj} is the loop gain of the outer voltage loop.

B. EQUIVALENT OUTPUT IMPEDANCE ANALYSIS OF TRADITIONAL CONTROL METHOD

The Bode diagrams of equivalent output impedances of traditional control method is shown in Fig. 7. The notch filter is not introduced, abbreviated as no notch filter. The notch filter is introduced to the grid-side inductor current feedback,

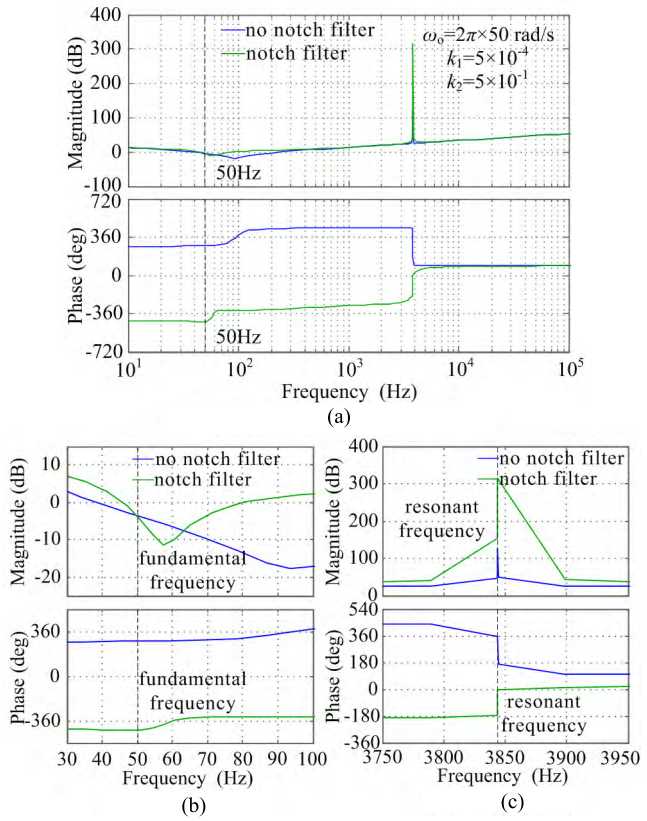

FIGURE 7. The Bode diagrams of equivalent output impedances of traditional control method. (a) Equivalent output impedance Z_{cpdj}. (b) Enlarged view. (c) Enlarged view.

abbreviated as notch filter. From Fig. 7(b), the equivalent output impedances in two cases are equivalent at the fundamental frequency, and the notch filter does not affect the fundamental current flowing into the grid. From Fig. 7(c), the equivalent output impedance of the former case exhibits a small value at the resonant frequency, which is not conducive to suppress the resonant peak. While, the equivalent output impedance of the latter case exhibits a large value. It can effectively suppress the resonant peak and avoid the high-frequency oscillation phenomenon.

C. STABILITY ANALYSIS OF TRADITIONAL CONTROL METHOD

The effect of bandwidth of notch filter on outer voltage loop stability is shown in Fig. 8. From Fig. 8(a), if the ratio of k_1 and k_2 is constant, the notch depth of notch filter is the same. However, with variation of k_1 and k_2, the bandwidth of notch filter will be changed. From Fig. 8(b) and Fig. 8(c), the system phase margin PM1 is 44.84° in the case of no notch filter. However, the system phase margin PM2-PM4 are reduced to approximately 25° in the case of notch filter. In order to ensure sufficient stability of the system in the weak grid, the system phase margin is usually required from 30° to 60° in [8]. Therefore, this requirement cannot be satisfied in the case of notch filter. At the same time, the bandwidth of notch filter has less impact on the stability of the system.

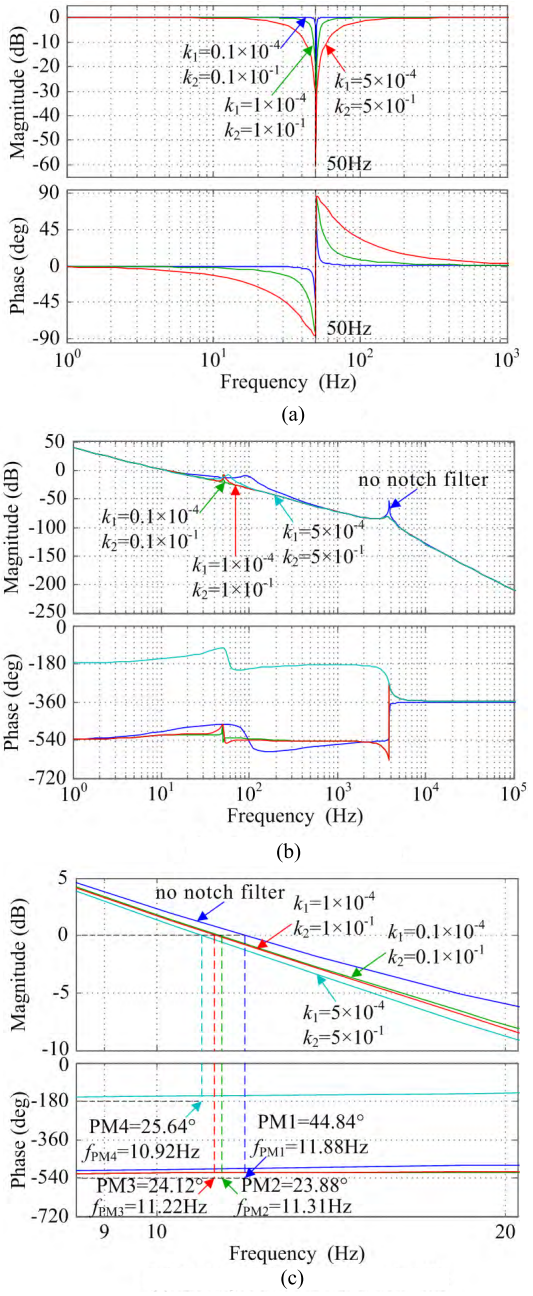

FIGURE 8. Effect of the bandwidth of notch filter on outer voltage loop stability. (a) Notch filter. (b) Open loop gain G_{opdj}. (c) Enlarged view at the banwidth.

The effect of notch depth of notch filter on outer voltage loop stability is shown in Fig. 9. From Fig. 9(a), if the ratio of k_1 and k_2 is adjusted, the notch depth of notch filter will be changed. From Fig. 9(b) and Fig. 9(c), the system phase margin PM1 is 44.84° in the case of no notch filter, however, system phase margin PM2-PM4 are reduced to approximately 25° in the case of notch filter. Therefore, the system phase margin cannot be satisfied the requirement in the weak grid in the case of notch filter. Meanwhile, the notch depth has less effect on the system stability.

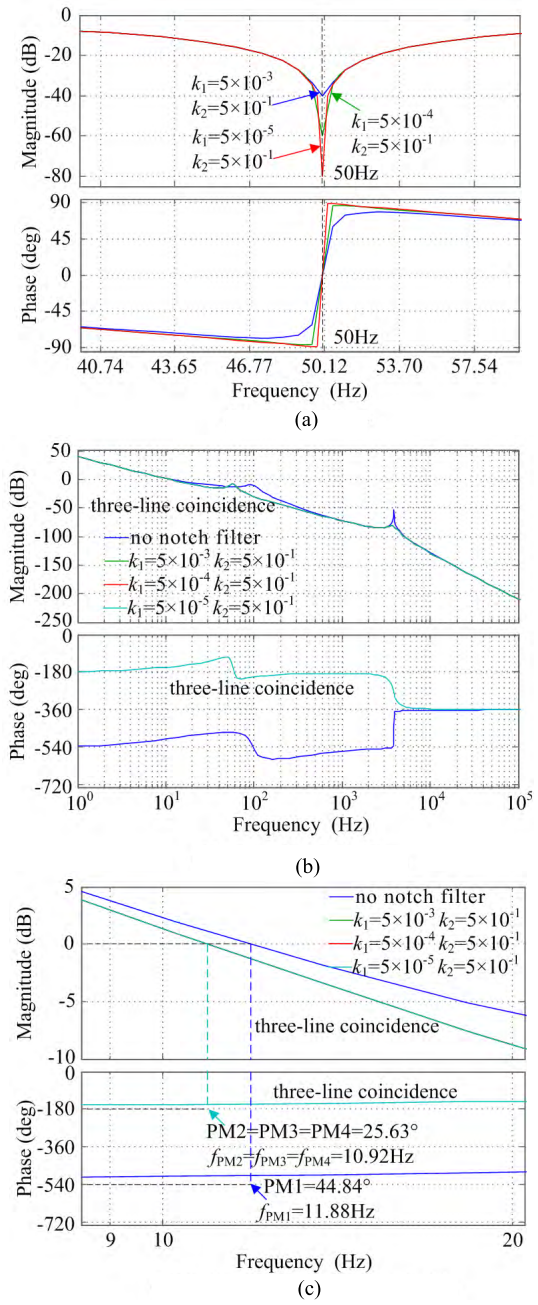

FIGURE 9. Effect of the notch depth of notch filter on outer voltage loop stability. (a) Notch filter. (b) Open loop gain G_{opdj}. (c) Enlarged view at the banwidth.

IV. PROPOSED OSCILLATION SUPPRESSION METHOD BY IMPROVED NOTCH FILTER

A. BASIC PRINCIPLES OF PROPOSED CONTROL METHOD

In order to solve the problem of stability reduction caused by traditional control method, the phase deviation introduced by the notch filter should be decreased. From (10), the phase deviation $\angle G_{\mathrm{Nd}}$ can be expressed as

$$\begin{aligned}\angle G_{\mathrm{Nd}} &= \angle G_{\mathrm{N}}(0) - \angle G_{\mathrm{N}}(j2\pi f) \\ &= 0 - \underbrace{(\arctan(\frac{2k_1 f/f_{\mathrm{o}}}{1-(f/f_{\mathrm{o}})^2})}_{\text{numerator}}\end{aligned}$$

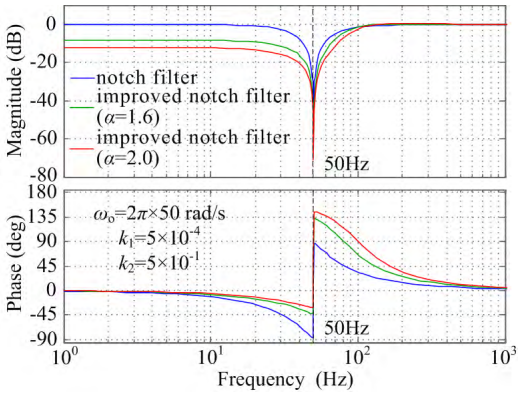

FIGURE 10. The Bode diagram of improved notch filter G_{mN}.

$$-\underbrace{\arctan(\frac{2k_2 f/f_{\mathrm{o}}}{1-(f/f_{\mathrm{o}})^2}))}_{\text{denominator}} \tag{13}$$

From (13), if the phase deviation $\angle G_{\mathrm{Nd}}$ is expected to decrease, it will be achieved by decreasing $\angle G_{\mathrm{N}}(0)$ or increasing $\angle G_{\mathrm{N}}(j2\pi f)$. It is difficult to change $\angle G_{\mathrm{N}}(0)$. Therefore, the target needs to be achieved by increasing $\angle G_{\mathrm{N}}(j2\pi f)$. The realization forms of increasing $\angle G_{\mathrm{N}}(j2\pi f)$ are divided into the increase of numerator phase or the decrease of denominator phase in (13). The two realization forms are equivalent, and both can achieve the target. Therefore, the improved notch filter is proposed to decrease the denominator phase, which introduces a deviation coefficient to the denominator of notch filter. Moreover, an adjustment coefficient should be added to remain the notch depth of notch filter unchanged. So the improved notch filter G_{mN} can be expressed as

$$G_{\mathrm{mN}} = \frac{1}{\alpha^2}\frac{(\frac{s}{2\pi f_{\mathrm{o}}})^2 + 2k_1\frac{s}{2\pi f_{\mathrm{o}}} + 1}{(\frac{s/\alpha}{2\pi f_{\mathrm{o}}})^2 + 2k_2\frac{s/\alpha}{2\pi f_{\mathrm{o}}} + 1} \tag{14}$$

where α is the deviation coefficient, it generally is greater than 1, and $1/\alpha^2$ is the adjustment coefficient.

The Bode diagram of improved notch filter G_{mN} is shown in Fig. 10. The case of notch filter is equivalent to the case of improved notch filter ($\alpha = 1.0$). Therefore, as the deviation coefficient α increases, the notch depth of improved notch filter remains the same at the characteristic frequency, but the phase deviation introduced by the improved notch filter decreases. It shows that the improved notch filter can meet the proposed requirements. In addition, the advantageous effects of improved notch filter on system stability are analyzed in Section IV.C.

The control block diagram of proposed control method by the improved notch filter is shown in Fig. 11, where $H_{\mathrm{mf}j}$ is the improved grid-side inductor current feedback coefficient, which contains the improved notch filter G_{mN}. From Fig. 11, the closed-loop transfer function of the inner current loop can be expressed as

$$i_{\mathrm{o}dj} = G_{\mathrm{mcpi}j} i_{\mathrm{odref}j} + i_{\mathrm{m}dj} - Y_{\mathrm{mcpi}j} u_{\mathrm{PCCd}} \tag{15}$$

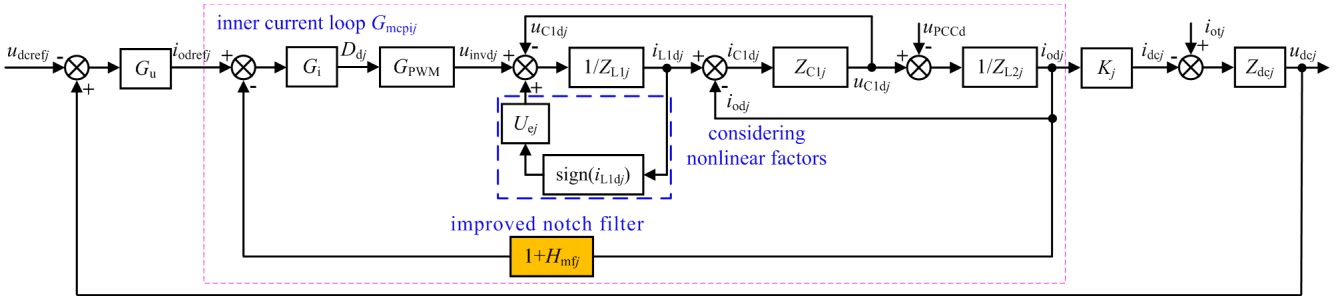

FIGURE 11. Control block diagram of proposed control method by the improved notch filter.

where G_{mcpij} is the improved equivalent coefficient of inner current loop, Y_{mcpij} is the improved equivalent admittance of inner current loop, and i_{mdj} is the improved controlled current source. They can be expressed as

$$\begin{cases} G_{mcpij} = \dfrac{G_i G_{PWM} Z_{C1j}}{F + H + J} \\ Y_{mcpij} = \dfrac{Z_{L1j} + Z_{C1j}}{F + H + J} \\ i_{mdj} = \dfrac{U_{ej}}{F + H + J} \cdot \text{sign}(i_{L1dj}) \end{cases} \tag{16}$$

where $F = Z_{L1j}Z_{L2j}$, $H = (1 + H_{mfj})G_i G_{PWM} Z_{C1j}$, and $J = Z_{C1j}(Z_{L1j} + Z_{L2j})$.

Analogous to the derivation process of traditional control method, the improved grid-side inductor current feedback coefficient H_{mfj} in the proposed control method can be expressed as

$$H_{mfj} = \frac{r_1 G_{mN}(Z_{L1j} + Z_{C1j})}{G_i G_{PWM} Z_{C1j}} \tag{17}$$

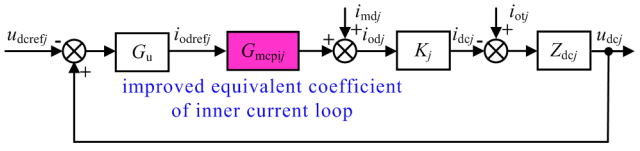

FIGURE 12. Simplified control block diagram of proposed control method.

The simplified control block diagram of proposed control method is shown in Fig. 12. As can be seen from Fig. 12, the double closed-loop transfer function of the system can be expressed as

$$u_{dcj} = G_{mcpdj} u_{dcrefj} + Z_{mdj} i_{mdj} - Z_{mcpdj} i_{otj} \tag{18}$$

where G_{mcpdj} is the improved equivalent coefficient of the double closed loop, Z_{mcpdj} is the improved equivalent impedance of the double closed loop, and Z_{mdj} is the improved equivalent impedance of controlled current source. They can be expressed as

$$\begin{cases} G_{mcpdj} = \dfrac{G_{mopdj}}{1 + G_{mopdj}} = \dfrac{G_u G_{mcpij} K_j Z_{dcj}}{1 + G_u G_{mcpij} K_j Z_{dcj}} \\ Z_{mcpdj} = \dfrac{Z_{dcj}}{1 + G_u G_{mcpij} K_j Z_{dcj}} \\ Z_{mdj} = \dfrac{K_j Z_{dcj}}{1 + G_u G_{mcpij} K_j Z_{dcj}} \end{cases} \tag{19}$$

where G_{mopdj} is the improved loop gain of the outer voltage loop.

B. EQUIVALENT OUTPUT IMPEDANCE ANALYSIS OF PROPOSED CONTROL METHOD

The Bode diagrams of equivalent output impedances of proposed control method is shown in Fig. 13. The improved notch filter is introduced to the grid-side inductor current feedback, abbreviated as improved notch filter. In the cases of notch filter, improved notch filter ($\alpha = 1.6$) and improved notch filter ($\alpha = 2.0$), it can be seen from Fig. 13(b) that the equivalent output impedances in three cases are equivalent at the fundamental frequency, and the improved notch filter has no effect on the fundamental current flowing into the grid. From Fig. 13(c), the equivalent output impedances of three cases exhibit a large value at the resonant frequency. Therefore, the proposed control method can achieve the same purpose, which can effectively suppress harmonic currents of parallel inverters flowing into the grid and avoid the high-frequency oscillation.

C. STABILITY ANALYSIS OF PROPOSED CONTROL METHOD

The effect of deviation coefficient of improved notch filter on outer voltage loop stability is shown in Fig. 14. In the case of notch filter, the system phase margin PM1 is 25.64°. In the case of improved notch filter ($\alpha = 1.6$), the system phase margin PM2 increases to 36.63° . In the case of improved notch filter ($\alpha = 2.0$), the system phase margin PM3 increases to 39.54°. Therefore, the system phase margin is between 30° and 60° using the proposed suppression method, which satisfies the condition that the system has sufficient stability in the weak grid. At the same time, with an increase in the deviation coefficient α, the system phase margin progressively raises, and the system stability gradually

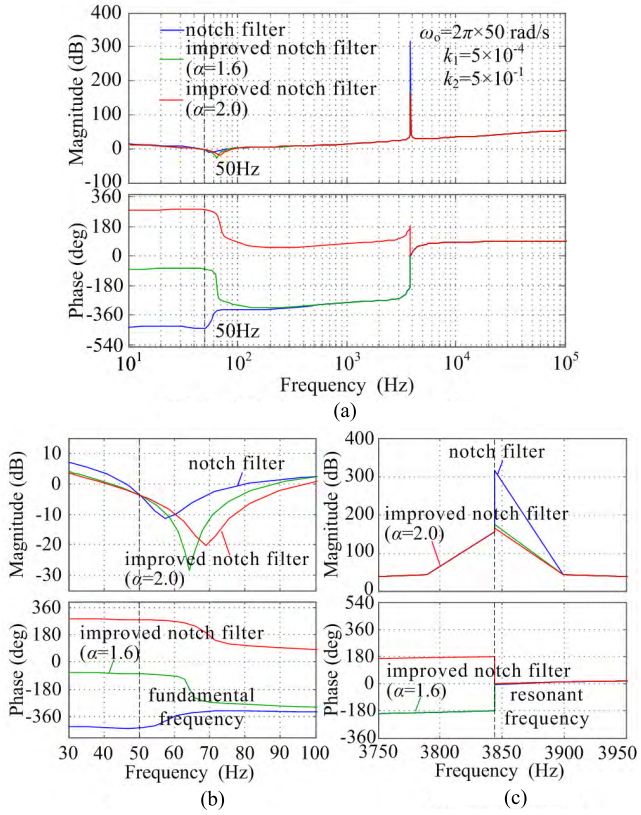

FIGURE 13. The Bode diagrams of equivalent output impedances of proposed control method. (a) Equivalent output impedance Z_{mcpdj}. (b) Enlarged view. (c) Enlarged view.

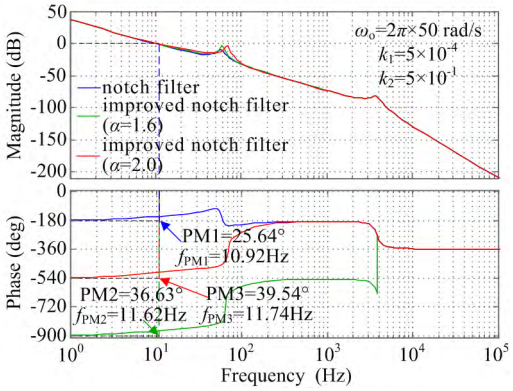

FIGURE 14. Effect of the deviation coefficient of improved notch filter on outer voltage loop stability.

is enhanced, which proves the effectiveness of the improved notch filter.

The Nyquist diagrams of the system are shown in Fig. 15. In the cases of notch filter, improved notch filter ($\alpha = 1.6$) and improved notch filter ($\alpha = 2.0$), the system phase margin PM1-PM3 presents 25.64°, 36.63°, and 39.54°, respectively. Therefore, the Nyquist criterion is basically consistent with the results obtained by the Bode in Fig. 14. Using the proposed suppression method, the system has sufficient stability in the weak grid.

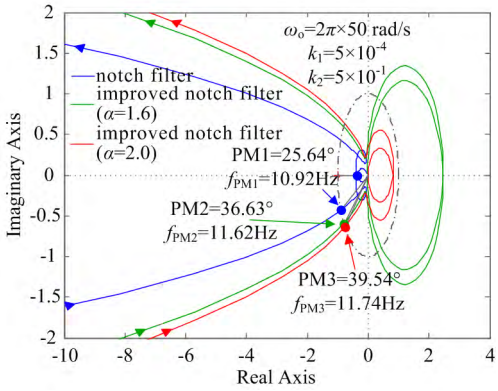

FIGURE 15. The Nyquist diagrams of the system.

V. PARAMETERS DESIGN OF IMPROVED NOTCH FILTER

The improved notch filter has four parameters: the characteristic frequency f_o, proportional coefficient k_1, proportional coefficient k_2, and deviation coefficient α. The specific design process is as follows:

1) The selection of characteristic frequency f_o: when the selected frequency away from the characteristic frequency f_o, the attenuation degree is drastically reduced. Therefore, the characteristic frequency f_o is set to the fundamental frequency.

2) Selection of k_1/k_2: in order to achieve the sufficient attenuation at the characteristic frequency f_o, the notch depth of the improved notch filter is generally selected to be -60dB. The amplitude $|G_{mN}(j2\pi f_o)|$ at the characteristic frequency f_o can be expressed as

$$|G_{mN}(j2\pi f_o)| = \frac{2k_1}{\sqrt{(\alpha^2-1)^2 + (2k_2\alpha)^2}} \tag{20}$$

3) Relationship between the deviation coefficient α and proportional coefficient k_2: if the improved notch filter has a narrow bandwidth and the cut-off frequency of the system is near the characteristic frequency f_o, the phase of improved notch filter at the cut-off frequency will be approximately equal to its phase at the characteristic frequency f_o. Therefore, $\angle G_{mN}(j2\pi f_o)$ is the phase of the improved notch filter at the characteristic frequency f_o, which can be expressed as

$$\angle G_{mN}(j2\pi f_o) = \frac{\pi}{2} - \arctan\left(\frac{2k_2\alpha}{\alpha^2-1}\right) \tag{21}$$

The relationship between the phase $\angle G_{mN}(j2\pi f_o)$ and deviation coefficient α is shown in Fig. 16. As the deviation coefficient α increases with $k_2 = 0.05$, the phase $\angle G_{mN}(j2\pi f_o)$ increases and approaches $\pi/2$. If the expected phase φ ranges from 0 to $\pi/2$, the relationship between the deviation coefficient α and proportional coefficient k_2 can be expressed as

$$k_2 = \tan(\frac{\pi}{2} - \varphi)\frac{\alpha^2-1}{2\alpha} \tag{22}$$

4) The selection of proportional coefficient k_1, proportional coefficient k_2 and deviation coefficient α: (14) can be

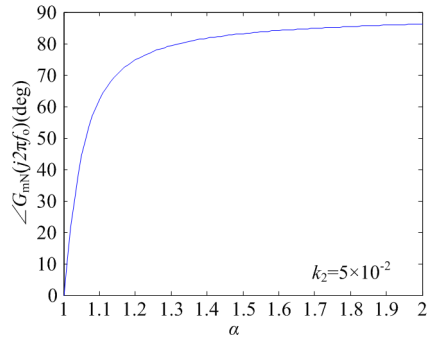

FIGURE 16. The relationship between the phase $\angle G_{mN}(j2\pi f_o)$ and deviation coefficient α.

rewritten as

$$G_{mN} = \frac{1}{\alpha^2}\frac{\left(\frac{s}{2\pi f_o}\right)^2 + 2\,x_1x_2\frac{\alpha^2-1}{2\alpha}\frac{s}{2\pi f_o} + 1}{\left(\frac{s}{\alpha 2\pi f_o}\right)^2 + 2\,x_2\frac{\alpha^2-1}{2\alpha}\frac{s}{\alpha 2\pi f_o} + 1} \tag{23}$$

where $x_1 = k_1/k_2$, and $x_2 = \tan(\pi/2\text{-}\varphi)$.

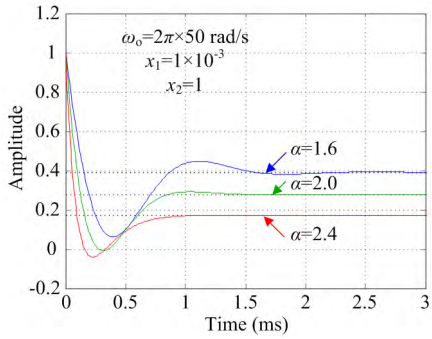

FIGURE 17. Step response of improved notch filter with different deviation coefficient α.

The step response of improved notch filter with different deviation coefficient α is shown in Fig. 17. As the deviation coefficient α increases, the undershoot gradually increases, and the adjustment time decreases little by little. Therefore, it is necessary to consider both the undershoot and adjustment time to select appropriate control parameters. If the deviation coefficient α is greater than 2.0, the undershoot is too large, so the value of α is less than or equal to 2.0.

VI. EXPERIMENTAL VERIFICATION

To verify the validity of theoretical analysis, an experimental platform for two parallel inverters system was built, as shown in Fig. 18. The experimental platform consists of the DC/DC converters, three-phase inverters and LCL filters. The control modes and filter parameters of two inverters are the same, as shown in Table 1.

A. IN CASE OF NO NOTCH FILTER

When two inverters are operating in parallel, the steady-state experimental waveforms of the PCC voltage u_{PCC} and

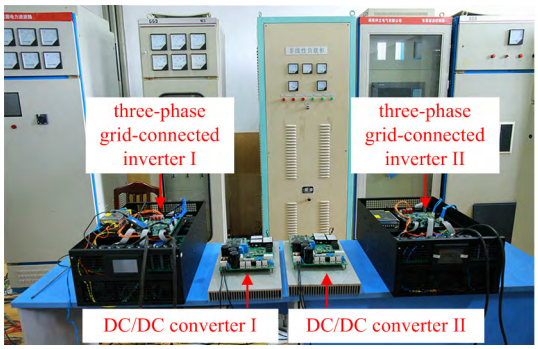

FIGURE 18. Experimental platform for multi-inverter grid-connected system.

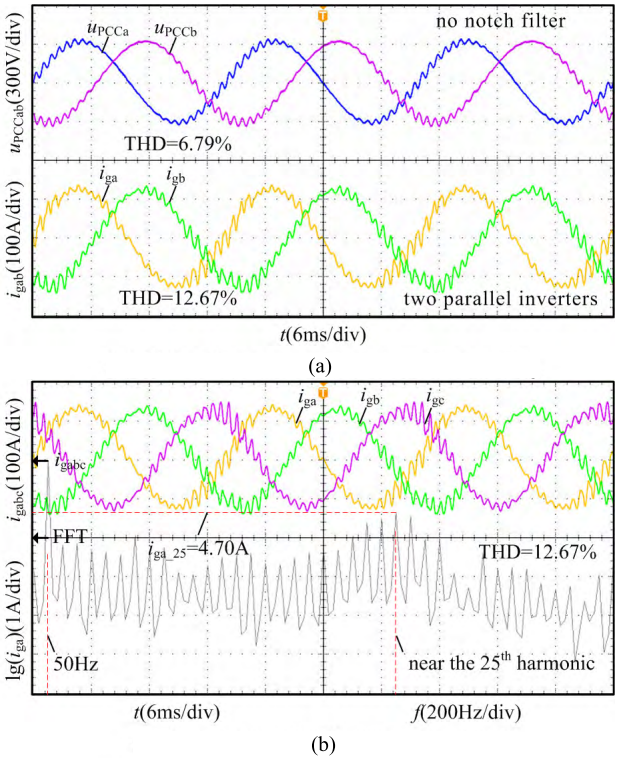

FIGURE 19. Experimental waveforms of PCC voltage u_{PCC} and grid-connected current i_g in the case of no notch filter. (a) PCC voltage u_{PCC} and grid-connected current i_g. (b) Spectrogram of grid -connected current i_g.

grid-connected current i_g in the case of no notch filter are shown in Fig. 19. The distortion rate of u_{PCC} is 6.79%, and the distortion rate of i_g is 12.67%. The resonant peak of i_g is 4.70A, and the resonant point of i_g is near the 25th harmonic (1250Hz). Therefore, the resonant phenomenon is obvious, and the reason is that the frequency of the harmonic current is equal to the parallel resonant frequency of impedance network, resulting in the parallel oscillation.

B. STEADY-STATE OPERATION

When two parallel inverters are operating in the case of notch filter, improved notch filter ($\alpha = 1.6$) and improved notch

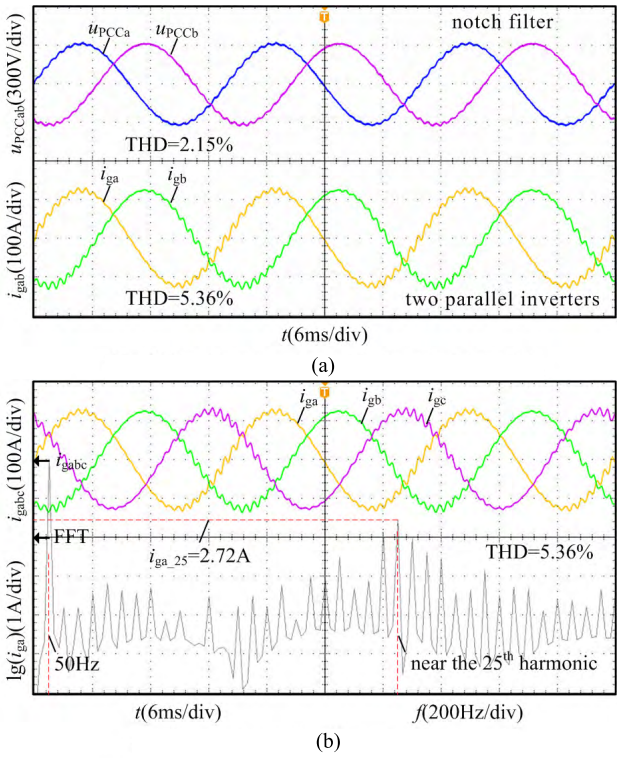

FIGURE 20. Steady-state experimental waveforms of PCC voltage u_{PCC} and grid-connected current i_g in the case of notch filter. (a) PCC voltage u_{PCC} and grid-connected current i_g. (b) Spectrogram of grid -connected current i_g.

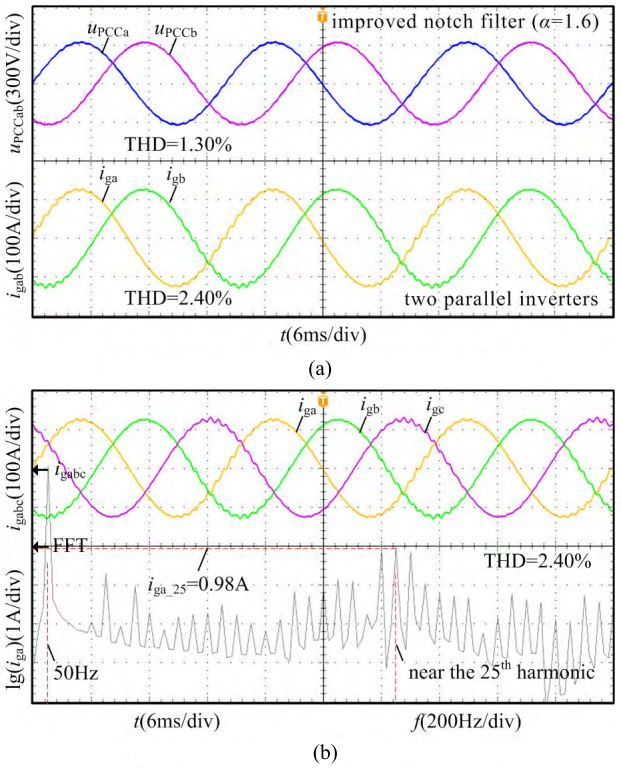

FIGURE 21. Steady-state experimental waveforms of u_{PCC} and i_g in the case of improved notch filter ($\alpha = 1.6$). (a) PCC voltage u_{PCC} and grid-connected current i_g. (b) Spectrogram of grid -connected current i_g.

TABLE 1. System parameters.

Parameter/Unit	value
Grid phase voltage U_g/V	220
Input inductance L_{dc1}/mH	5
DC-side capacitor C_{dc1}/μF	1×10^4
Inverter-side inductance L_1/mH, R_{L1}/Ω	2, 0.002
Grid-side inductance L_2/mH, R_{L2}/	0.8, 0.001
Grid impedance L_g/mH	2
Outer voltage loop proportional coefficient k_{pu}	0.8
Outer voltage loop integral coefficient k_{iu}	60
Inner current loop proportional coefficient k_{pi}	0.45
Inner current loop integral coefficient k_{ii}	1000
Characteristic frequency f_o/Hz	50
Characteristic angle frequency ω_o/rad/s	314
Proportional coefficient k_1, k_2	5×10^{-4}, 5×10^{-1}
Proportional coefficient r_1	15

filter ($\alpha = 2.0$), the steady-state experimental waveforms of the PCC voltage u_{PCC} and grid-connected current i_g are shown in Fig. 20, Fig. 21 and Fig. 22. In addition, experimental results of the PCC voltage u_{PCC} and grid-connected current i_g in three cases mentioned above are shown in Table 2.

In the case of notch filter from Fig. 20, the distortion rate of u_{PCC} is 2.15%, and the distortion rate of i_g is 5.36%. The resonant peak of i_g is 2.72A, and the resonant point of i_g is near the 25th harmonic (1250Hz). The reason is that the damping of the system is not sufficient, and the harmonic amplification occurs.

TABLE 2. Experimental results of the PCC voltage u_{PCC} and grid-connected current i_g with two parallel inverters.

Case	THD of u_{PCC}	THD of i_g	Resonant peak and resonant point of i_g
notch filter	2.15%	5.36%	2.72A 25th harmonic
improved notch filter (α=1.6)	1.30%	2.40%	0.98A 25th harmonic
improved notch filter (α=2.0)	1.26%	2.14%	0.82A 25th harmonic

In the case of improved notch filter ($\alpha = 1.6$) from Fig. 21, the distortion rate of u_{PCC} is 1.30%, and the distortion rate of i_g is 2.40%. The resonant peak of i_g is 0.98A, and the resonant point of i_g is near the 25th harmonic (1250Hz). In the case of improved notch filter ($\alpha = 2.0$) from Fig. 22, the distortion rate of u_{PCC} is 1.26%, and the distortion rate of i_g is 2.14%. The resonant peak of i_g is 0.82A, and the resonant point of i_g is near the 25th harmonic (1250Hz). Due to the introduction of sufficient damping in the impedance network, the system can operate stably in the two cases mentioned above.

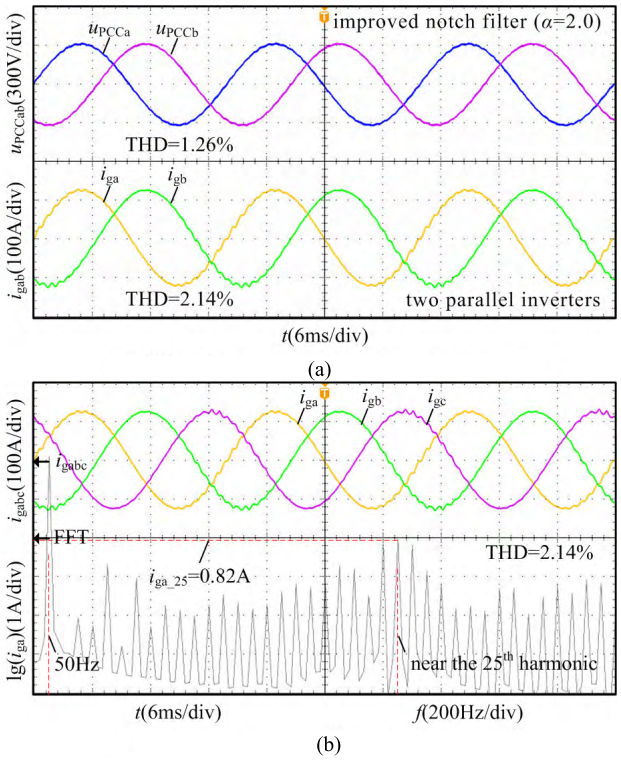

FIGURE 22. Steady-state experimental waveforms of u_{PCC} and i_g in the case of improved notch filter ($\alpha = 2.0$). (a) PCC voltage u_{PCC} and grid-connected current i_g. (b) Spectrogram of grid -connected current i_g.

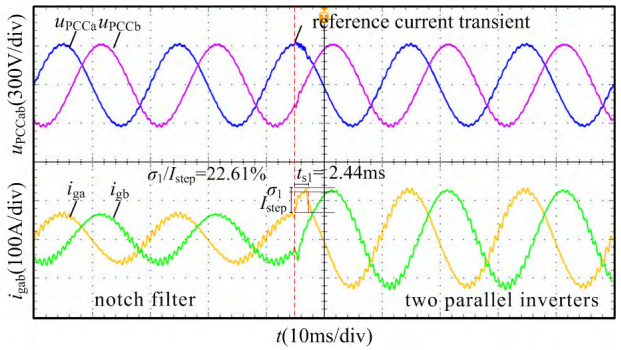

FIGURE 23. Dynamic experimental waveforms of PCC voltage u_{PCC} and grid-connected current i_g in the case of notch filter.

C. DYNAMIC OPERATION

When two inverters are operating in parallel, the root mean square (RMS) value of reference grid-side inductor current i_{oj}ref increases from 18.75A to 37.5A for each grid-connected inverter. Therefore, the RMS of reference grid-connected current i_{gref} raises from 37.5A to 75A. In the cases of notch filter, improved notch filter ($\alpha = 1.6$) and improved notch filter ($\alpha = 2.0$), experimental waveforms of PCC voltage u_{PCC} and grid-connected current i_g during reference current transient are shown in Fig. 23, Fig. 24 and Fig. 25. Moreover, experimental results of the overshoot and adjustment time of

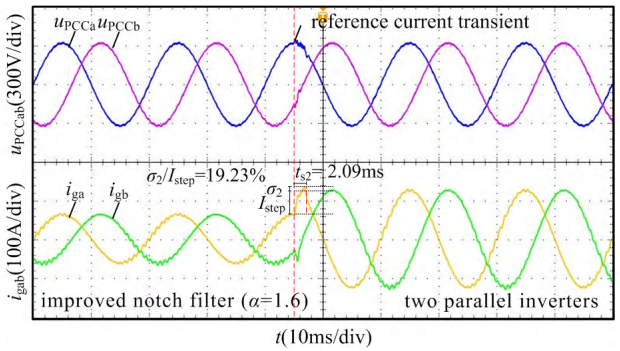

FIGURE 24. Dynamic experimental waveforms of u_{PCC} and i_g in the case of improved notch filter ($\alpha = 1.6$).

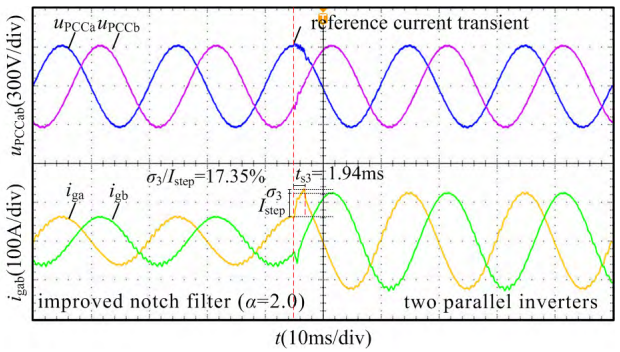

FIGURE 25. Dynamic experimental waveforms of u_{PCC} and i_g in the case of improved notch filter ($\alpha = 2.0$).

TABLE 3. Experimental results of the overshoot and adjustment time of grid-connected current i_g with two parallel inverters.

Case	Overshoot of i_g	Adjustment time of i_g
notch filter	22.61%	2.44ms
improved notch filter (α=1.6)	19.23%	2.09ms
improved notch filter (α=2.0)	17.35%	1.94ms

grid-connected current i_g in three cases mentioned above are shown in Table 3.

VII. CONCLUSION

In order to solve the problem of stability reduction caused by traditional control method, a stability enhancement method by the improved notch filter is proposed for parallel grid-connected inverters. The conclusions are summarized as following.

I) The proposed control method can change the impedance properties of the grid-connected inverter. It effectively restrains parallel inverters' harmonic current into the grid, and avoids the high-frequency oscillation of impedance network. Moreover, it can improve the phase margin of the system, and ensure the sufficient stability of the system in the weak grid.

II) Considering the notch depth and dynamic performance of improved notch filter, the appropriate control parameters

are selected. It provides guidelines for the design of improved notch filter.

REFERENCES

[1] X. Guo, Y. Yang, and T. Zhu, "ESI: A novel three-phase inverter with leakage current attenuation for transformerless PV systems," *IEEE Trans. Ind. Electron.*, vol. 65, no. 4, pp. 2967–2974, Apr. 2018.
[2] N. M. Nor, A. Ali, T. Ibrahim, and M. F. Romlie, "Battery storage for the utility-scale distributed photovoltaic generations," *IEEE Access*, vol. 6, pp. 1137–1154, Nov. 2018.
[3] M. Abedini, M. Davarpanah, and M. Sanaye-Pasand, "Appropriate grounding system for grid-connected small-scale synchronous generators," *IEEE Trans. Ind. Appl.*, vol. 51, no. 6, pp. 5390–5397, Nov./Dec. 2015.
[4] D. Remon, A. M. Cantarellas, and P. Rodriguez, "Equivalent model of large-scale synchronous photovoltaic power plants," *IEEE Trans. Ind. Appl.*, vol. 52, no. 6, pp. 5029–5040, Nov./Dec. 2016.
[5] M. H. Hany, "Whale optimisation algorithm for automatic generation control of interconnected modern power systems including renewable energy sources," *IET Gener. Transm. Distrib.*, vol. 12, no. 3, pp. 607–614, Feb. 2018.
[6] A. H. Azizi and M. Rahimi, "Dynamic performance analysis, stability margin improvement and transfer power capability enhancement in DFIG based wind turbines at weak AC grid conditions," *Int. J. Elect. Power Energy Syst.*, vol. 99, pp. 434–446, Jul. 2018.
[7] X. Li, J. Fang, Y. Tang, and X. Wu, "Robust design of LCL filters for single-current-loop-controlled grid-connected power converters with unit pcc voltage feedforward," *IEEE J. Emerg. Sel. Top. Power Electron.*, vol. 6, no. 1, pp. 54–72, Mar. 2018.
[8] L. Yang *et al.*, "Effect of phase-locked loop on small-signal perturbation modelling and stability analysis for three-phase LCL-type inverter connected to weak grid," *IET Renew. Power Gener.*, vol. 13, no. 1, pp. 86–93, Jan. 2019.
[9] X. Guo, Y. Yang, and X. Wang, "Advanced control of grid-connected current source converter under unbalanced grid voltage conditions," *IEEE Trans. Ind. Electron.*, vol. 65, no. 12, pp. 9225–9233, Dec. 2018.
[10] Y. Yang, Q. Ye, L. J. Tung, M. Greenleaf, and H. Li, "Integrated size and energy management design of battery storage to enhance grid integration of large-scale PV power plants," *IEEE Trans. Ind. Electron.*, vol. 65, no. 1, pp. 394–402, Jan. 2018.
[11] H. Cai, R. Zhao, and H. Yang, "Study on ideal operation status of parallel inverters," *IEEE Trans. Power Electron.*, vol. 23, no. 6, pp. 2964–2969, Nov. 2008.
[12] J. He, Y. W. Li, D. Bosnjak, and B. Harris, "Investigation and active damping of multiple resonances in a parallel-inverter-based microgrid," *IEEE Trans. Power Electron.*, vol. 28, no. 1, pp. 234–246, Jan. 2013.
[13] M. Borrega, L. Marroyo, R. González, J. Balda, and J. L. Agorreta, "Modeling and control of a master–slave PV inverter with N-paralleled inverters and three-phase three-limb inductors," *IEEE Trans. Power Electron.*, vol. 28, no. 6, pp. 2842–2855, Jun. 2013.
[14] J. L. Agorreta, M. Borrega, J. López, and L. Marroyo, "Modeling and control of N-paralleled grid-connected inverters with LCL filter coupled due to grid impedance in PV plants," *IEEE Trans. Power Electron.*, vol. 26, no. 3, pp. 770–785, Mar. 2011.
[15] F. Wang, J. L. Duarte, M. A. M. Hendrix, and P. F. Ribeiro, "Modeling and analysis of grid harmonic distortion impact of aggregated DG inverters," *IEEE Trans. Power Electron.*, vol. 26, no. 3, pp. 786–797, Mar. 2011.
[16] J. H. R. Enslin and P. J. M. Heskes, "Harmonic interaction between a large number of distributed power inverters and the distribution networks," *IEEE Trans. Power Electron.*, vol. 19, no. 6, pp. 1586–1593, Nov. 2004.
[17] D. Remon, A. M. Cantarellas, J. M. Mauricio, and P. Rodriguez, "Power system stability analysis under increasing penetration of photovoltaic power plants with synchronous power controllers," *IET Renew. Power Gener.*, vol. 11, no. 6, pp. 733–741, May 2017.
[18] X. Wang, F. Blaabjerg, M. Liserre, Z. Chen, J. He, and Y. Li, "An active damper for stabilizing power-electronics-based AC systems," *IEEE Trans. Power Electron.*, vol. 29, no. 7, pp. 3318–3329, Jul. 2014.
[19] C. Zheng, L. Zhou, B. Xie, Q. Zhang, and H. Li, "A stabilizer for suppressing harmonic resonance in multi-parallel inverter system," in *Proc. IEEE Transp. Electrific. Conf. Expo (ITEC Asia–Pacific)*, Aug. 2017, pp. 1–6.
[20] S. Zhang, S. Jiang, X. Lu, B. Ge, and F. Z. Peng, "Resonance issues and damping techniques for grid-connected inverters with long transmission cable," *IEEE Trans. Power Electron.*, vol. 29, no. 1, pp. 110–120, Jan. 2014.
[21] N. A. Rufa'i, L. Zhang, and B. Chong, "Performance analysis of adaptive notch filter active damping methods for grid-connected converters under a varying grid impedance," in *Proc. IEEE Manchester PowerTech*, Jun. 2017, pp. 1–6.
[22] S.-G. Jeong and M.-H. Park, "The analysis and compensation of dead-time effects in PWM inverters," *IEEE Trans. Ind. Electron.*, vol. 38, no. 2, pp. 108–114, Apr. 1991.

LING YANG (S'16) was born in Liaoning, China, in 1992. She received the B.S. degree from the College of Electrical and Information Engineering, Hunan University, Changsha, China, in 2014, where she is currently pursuing the Ph.D. degree in electrical engineering.

Her research interests include power electronics and distributed power systems.

YANDONG CHEN (S'13–M'14–SM'18) was born in Hunan, China, in 1979. He received the B.S. and M.S. degrees in instrument science and technology and the Ph.D. degree in electrical engineering from Hunan University, Changsha, China, in 2003, 2006, and 2014, respectively, where he has been an Associate Professor with the College of Electrical and Information Engineering.

His research interests include power electronics for microgrid, distributed generation, power supply, and energy storage. He is a Senior Member of the IEEE PES & PELS. He was a recipient of the 2014 National Technological Invention Awards of China, and the 2014 WIPO-SIPO Award for Chinese Outstanding Patented Invention.

AN LUO (SM'09) was born in Changsha, China, in 1957. He received the B.S. and M.S. degrees in industrial automation from Hunan University, Changsha, in 1982 and 1986, respectively, and the Ph.D. degree in fluid power transmission and control from Zhejiang University, Hangzhou, China, in 1993. From 1996 to 2002, he was a Professor with Central South University. Since 2003, he has been a Professor with the College of Electrical and Information Engineering, Hunan University, where he also serves as the Chief of the National Electric Power Conversion and Control Engineering Technology Research Center.

His research interests include distributed generation, microgrid, and power quality. He was elected to the Chinese National Academy of Engineering (CNAE), in 2015, the highest honor for scientists and engineers and scientists in China. He received the highly prestigious China National Science and Technology Awards three times (2006, 2010, and 2014).

KUNSHAN HUAI was born in Henan, China, in 1991. He received the B.S. and M.S. degrees from the College of Electrical and Information Engineering, Hunan University, Changsha, China, in 2014 and 2017, respectively. He is currently with Guangzhou Power Supply Co., Ltd., Guangzhou, China.

His research interests include power electronics and distributed power systems.